

Investigation of laminar dispersion with optical coherence tomography and optical Doppler tomography

Yeh-Chan Ahn, Woonggyu Jung, Jun Zhang, and Zhongping Chen

Department of Biomedical Engineering and Beckman Laser Institute, University of California, Irvine, CA 92612
ahny@uci.edu, jungw@uci.edu, junzhang@uci.edu, z2chen@uci.edu

<http://chen.bli.uci.edu>

Abstract: Laminar dispersion in a serpentine microchannel with a Y-shape inlet was investigated using optical coherence tomography (OCT) and optical Doppler tomography (ODT). Dimensionless analysis was performed to understand the complex convective diffusion phenomena. It was shown that OCT/ODT is not only a visualization method but also a methodology to characterize important physics: streamwise velocity, secondary streamline, sedimentation time scale, shear dispersion. To demonstrate the capability of OCT/ODT, transient mixing was observed and three-dimensional imaging was performed.

©2005 Optical Society of America

OCIS codes: (110.4500) Optical coherence tomography; (280.2490) Flow diagnostics

References and links

1. R. H. Liu, M. A. Stremler, K. V. Sharp, M. G. Olsen, J. G. Santiago, R. J. Adrian, H. Aref, and D. J. Beebe, "Passive mixing in a three-dimensional serpentine microchannel," *J. MEMS* **9**, 190-197 (2000).
2. A. D. Stroock, S. K. W. Dertinger, A. Ajdari, I. Mezic, H. A. Stone, and G. M. Whitesides, "Chaotic mixer for microchannels," *Science* **295**, 647-651 (2002).
3. M. Koch, H. Witt, A. G. R. Evans, and A. Brunnschweiler, "Improved characterization technique for micromixers," *J. Micromech. Microeng.* **9**, 156-158 (1999).
4. D. J. Beebe, R. J. Adrian, M. G. Olsen, M. A. Stremler, H. Aref, and B. H. Jo, "Passive mixing in microchannels: Fabrication and flow experiments," *Mec. Ind.* **2**, 343-348 (2001).
5. T. J. Johnson, D. Ross, and L. E. Locascio, "Rapid microfluidic mixing," *Anal. Chem.* **74**, 45-51 (2002).
6. Y. Sato, G. Irisawa, M. Ishizuka, K. Hishida, and M. Maeda, "Visualization of convective mixing in microchannel by fluorescence imaging," *Meas. Sci. Technol.* **14**, 114-121 (2003).
7. D. Huang, E. A. Swanson, C. P. Lin, J. S. Schuman, W. G. Stinson, W. Chang, M. R. Hee, T. Flotte, K. Gregory, C. A. Puliafito, *et al.*, "Optical coherence tomography," *Science* **254**, 1178-1181 (1991).
8. Z. Chen, T. E. Miller, S. Srinivas, X. J. Wang, A. Malekafzali, M. J. C. van Gemert, and J. S. Nelson, "Noninvasive imaging of in vivo blood flow velocity using optical Doppler tomography," *Opt. Lett.* **22**, 1119-1121 (1997), <http://ol.osa.org/ViewMedia.cfm?id=36250&seq=0>.
9. Y. Zhao, Z. Chen, C. Saxer, S. Xiang, J. F. de Boer, and J. S. Nelson, "Phase-resolved optical coherence tomography and optical Doppler tomography for imaging blood flow in human skin with fast scanning speed and high velocity sensitivity," *Opt. Lett.* **25**, 114-116 (2000), <http://ol.osa.org/ViewMedia.cfm?id=291&seq=0>.
10. V. Westphal, S. Yazdanfar, A. M. Rollins, and J. A. Izatt, "Real-time, high velocity-resolution color Doppler optical coherence tomography," *Opt. Lett.* **27**, 34-36 (2002), <http://ol.osa.org/ViewMedia.cfm?id=67270&seq=0>.
11. L. Wang, W. Xu, M. Bachman, G. P. Li, and Z. Chen, "Phase-resolved optical Doppler tomography for imaging flow dynamics in microfluidic channels," *Appl. Phys. Lett.* **85**, 1855-1857, (2004).
12. R. K. Wang, "High-resolution visualization of fluid dynamics with Doppler optical coherence tomography," *Meas. Sci. Technol.* **15**, 725-733 (2004).
13. C. Xi, D. L. Marks, D. S. Parikh, L. Raskin, and S. A. Boppart, "Structural and functional imaging of 3D microfluidic mixers using optical coherence tomography," *PNAS* **101**, 7516-7521 (2004).
14. W. R. Dean, "Note on the motion of fluid in a curved pipe," *Phil. Mag.* **4**, 208-223 (1927).
15. W. R. Dean, "The stream-line motion of fluid in a curved pipe," *Phil. Mag.* **5** 673-695 (1928).

16. M. E. Erdogan and P. C. Chatwin, "The effects of curvature and buoyancy on the laminar dispersion of solute in a horizontal tube," *J. Fluid Mech.* **29**, 465-484 (1967).
17. R. J. Nunge, T. S. Lin, and W. N. Gill, "Laminar dispersion in curved tubes and channels," *J. Fluid Mech.* **51**, 363-383 (1972).
18. M. Johnson and R. D. Kamm, "Numerical studies of steady flow dispersion at low Dean number in a gently curving tube," *J. Fluid Mech.* **172**, 329-345 (1986).
19. N. S. Reejhsinghani, W. N. Gill, and A. J. Barduhn, "Part III. Experiments in horizontal tubes including observations on natural convection effects," *AIChE J.* **12**, 916-921 (1966).
20. P. B. Rhines and W. R. Young, "How rapidly is a passive scalar mixed within closed streamlines?," *J. Fluid Mech.* **133**, 133-145 (1983).
21. G. J. Tearney, B. E. Bouma, and F. G. Fujimoto, "High-speed phase- and group-delay scanning with a grating-based phase control delay line," *Opt. Lett.* **22**, 1811-1813 (1997), <http://ol.osa.org/ViewMedia.cfm?id=36459&seq=0>.
22. A. M. Rollins, M. D. Kulkarnis, S. Yazdanfar, R. Ung-arunyawee, and J. A. Izatt, "In vivo video rate optical coherence tomography," *Opt. Express* **3**, 219-229 (1998), <http://www.opticsexpress.org/abstract.cfm?URI=OPEX-3-6-219>.

1. Introduction

Two-fluid mixing is ubiquitous in microfluidic devices for biomedical and biochemical processes. Several shapes of microfluidic mixers have been reported; squarewave mixer [1], three-dimensional serpentine mixer [1], staggered herringbone mixer [2] etc. The mixing efficiency that determines the performance of a microfluidic mixer is one of the most important parameters. Great efforts have been made to achieve rapid and effective mixing even in laminar flow. Flow visualization methods, such as light microscopy and confocal microscopy have been utilized to monitor and evaluate the mixing performance of a mixer [1-6]. The light microscopy produces *en face* images but cannot resolve depth information. The confocal microscopy, which uses a high numerical beam, gives high-resolution cross-sectional images. However, the imaging depth is limited within $\sim 100\ \mu\text{m}$. In addition, both methods cannot provide structural and velocity information simultaneously.

Optical coherence tomography (OCT) is an emerging high-resolution medical imaging technology [7]. OCT detects back-scattered light from the sample and performs depth discrimination by using the coherence gating technique of low-coherence interferometry. Frequently, OCT is compared to ultrasound imaging technique. However, OCT provides higher depth resolution ($1\sim 10\ \mu\text{m}$) because it utilizes a broadband light source instead of sound waves. Similar to the Doppler ultrasound, which uses the Doppler frequency shift of the sound wave reflected by a moving particle, OCT can be modified to the optical Doppler tomography (ODT). ODT can visualize the velocity distribution of moving particles [8-10].

The lateral resolution of OCT/ODT is determined by the transfer function of focusing optics similar to the case of imaging optics. The higher numerical aperture beam gives a better lateral resolution. The depth resolution of OCT/ODT is mainly determined by the optical bandwidth of the light beam and decoupled from the lateral one. Therefore, high depth resolution is possible even at sites not accessible by a high numerical aperture beam. Near-infrared wavelength beam is generally used as a light source for OCT to increase the penetration depth (few millimeters) through highly scattering media or tissues. In addition, it is an *in vivo* and non-invasive technique having a high dynamic range and a good sensitivity ($> 100\ \text{dB}$). Because of such outstanding properties, OCT/ODT is known as an ideal tool for achieving the simultaneous image of the structure and the velocity distribution of a sample. However, only a few applications to a microfluidic device have been reported [11-13].

In this paper, the effect of secondary flow and buoyancy on the laminar dispersion in a serpentine microchannel with a square cross-section was investigated using OCT/ODT. When a neutrally buoyant solute is injected into a straight microchannel through which a solvent is in laminar flow, dispersion depends only on molecular diffusion and advection with the streamwise flow. However, additional complexity arises when secondary flow is present and/or the solute is not neutrally buoyant. The secondary flow in a transverse plane is usually generated by curving a pipe and has two counter-rotating vortices [14-15]. It enhances

transverse mixing and, thus, is less effective in dispersing the solute longitudinally relative to the Poiseuille flow in a straight pipe [16-18]. The effect of buoyancy caused by a density difference between solute and solvent also contributes to the generation of secondary flow [16, 19]. Previous studies presume infinite time and a uniformly, gently curved pipe (the ratio of pipe to coil radius is constant and approaching to 0). However, transient and steady-state flows in a serpentine microchannel, which has a varying curvature and is not gently curved, are of concern to us here. While theoretical and numerical methods are not easily applicable to the present situation, OCT/ODT can provide an excellent visualization even in such a complex situation.

2. Nondimensional analysis and experimental setup

A Polymethyl methacrylate (PMMA) microfluidic channel was fabricated. It had two inlets connected with a Y-shape coupler and the serpentine channel followed the coupler as shown in Fig. 1. The dimension of cross-section was $600\ \mu\text{m} \times 600\ \mu\text{m}$ and the radius of curvature was 1.7 mm. Two-fluid mixing was produced by injection of deionized water through one inlet and scattering particle/water mixture (10 % volume concentration) through the other. Scattering particles were polystyrene beads which have a $0.5\ \mu\text{m}$ mean diameter and $1.05\ \text{g/cc}$ density. Each fluid was injected with the same flow rate and controlled by a dual-syringe pump (Harvard Apparatus 11 Plus, Holliston, MA) with $\pm 0.5\%$ flow rate accuracy.

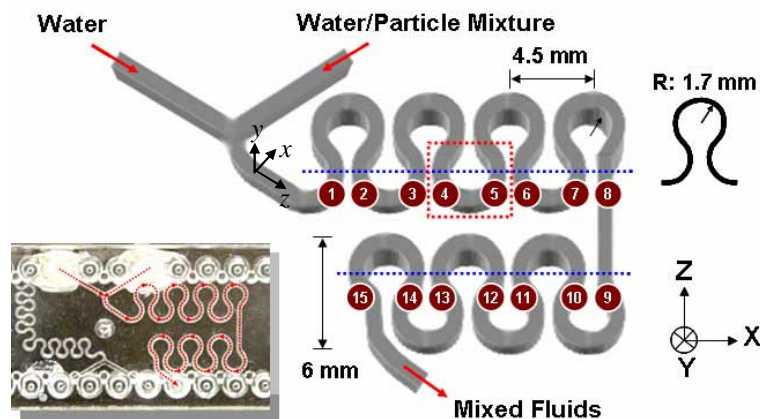


Fig. 1. Serpentine microfluidic channel with Y-shape inlet. Blue lines denote scan lines by OCT/ODT. Cross sections cut by the scan line are numbered from 1 to 15. Red box indicates scan area for three-dimensional volume imaging.

For small particles in a steady, fully developed water flow through a square, straight microchannel, the convective diffusion equation which describes the concentration distribution in dimensionless form becomes

$$\frac{\partial c}{\partial t} + Pe \left[w \frac{\partial c}{\partial z} \right] = \nabla^2 c \quad (1)$$

where c is particle concentration, w is velocity component along streamwise (z) direction, and Pe is Peclet number, which is Reynolds number Re times Schmidt number Sc . Reynolds number, which is the only parameter governing flow, is defined as $Re = UW/\nu$, where U is the average streamwise velocity, W is the width of the channel, and ν is the kinematic viscosity of water. Schmidt number is defined as $Sc = \nu/D$, where D is the molecular diffusivity of particle with respect to water. Therefore, the mixing is governed by the Reynolds number and Peclet number.

The mixing in a curved channel is also affected by secondary flow which depends on the Reynolds number and Dean number Dn [14]. The Dean number is defined as $Dn = Re^{1/2} (W/R)$, where R is the radius of curvature. The convective diffusion equation for the low Dean number is similar to Eq. (1) in dimensionless form:

$$\frac{\partial c}{\partial t} + Sc \left[u \frac{\partial c}{\partial x} + v \frac{\partial c}{\partial y} \right] + Pe \left[w \frac{\partial c}{\partial z} \right] = \nabla^2 c \quad (2)$$

where u and v are transverse velocity components which are normal to streamwise (z) direction [Note that three-dimensional velocity field (u,v,w) has two counter-rotating sets of helical streamlines]. Hence, it can be inferred that the mixing performance in the current serpentine channel is at least a function of the Reynolds number, Dean number, and Peclet number (or Schmidt number). If particle density is larger than water, sedimentation occurs by buoyancy force and accompanies secondary flow. Sedimentation is represented by sedimentation number $N_G = 2a^2 \Delta \rho g / 9 \mu U$ which is defined as the ratio of sedimentation velocity ($2a^2 \Delta \rho g / 9 \mu$) to average streamwise velocity or the ratio of buoyancy to inertial force. Density difference is denoted by $\Delta \rho$, gravitational acceleration by g , dynamic viscosity of water by μ , particle radius by a . The ranges of dimensionless numbers for the downstream of the Y-junction are listed in Table 1.

Table 1. Flow Conditions

Dimensionless Numbers	Run 1	Run 2	Run 3	Run 4	Run 5
Re	0.17	0.28	0.39	0.61	0.83
$Sc (\times 10^6)$			1.17		
$Pe (\times 10^5)$	1.95	3.25	4.54	7.14	9.74
Dn	0.10	0.16	0.23	0.36	0.49
$N_G (\times 10^{-5})$	2.52	1.51	1.08	0.69	0.51

The current experimental conditions were definitely in laminar flow regime ($Re \ll 100$). The curvature ratio W/R varied periodically with large amplitude (from -35 % to 35 %) along the streamwise direction so that the first order of Dean's solution for secondary flow velocity was not exactly applicable to the present cases. However, the solution gave the order of magnitude of secondary flow velocity. The maximum secondary flow velocity relative to average streamwise velocity was $0.014 Dn^2 / Re$ [15]. Therefore, the secondary flow velocity was much smaller than average streamwise velocity. In the transverse plane (x - y plane), it was worthwhile to compare turnover, homogenization, and diffusion times [20]. Turnover time is the circulation time of a particle traveling around the secondary flow streamline. Homogenization time is the time scale for mixing along the secondary flow streamline. Initial values of concentration at any point on the secondary flow streamline will be replaced by its average along the streamline. Diffusion time is the time scale for mixing across the secondary flow streamline which is caused by the concentration gradient between two proximal streamlines. At high $Dn^2 Sc$, the turnover and homogenization times are much smaller than the diffusion time and, thus, the isoconcentration lines approach secondary flow streamlines [18].

A schematic of the OCT/ODT system is illustrated in Fig. 2. Light was coupled into the 2x2 fiber coupler and split into a sample and reference arm. Since low-coherence interferometry was based on the interference, a broadband super-luminescent diode laser was used and delivered an output power of 10 mW at a central wavelength of 1310 nm with a bandwidth of 70 nm. A visible aiming beam (633 nm) was used to locate the exact imaging position on the sample. Reflected beams from the two arms of the interferometer were recombined and detected on a photodetector.

In the reference arm, a rapid-scanning optical delay line was used that employed a grating to control the phase and group delays separately so that no phase modulation was generated

when the group delay was scanned [21-22]. It performed continuous depth scanning (A-scan) with 500 Hz. Phase modulation in the reference arm was generated by an electro-optic phase modulator that produced a carrier frequency (500 kHz).

In the sample arm, a collimated beam was focused on the sample through the objective lens. In order to synthesize a three-dimensional image, additional two-axis scanning was needed and established by two moving stages. The probing beam had a 10 μm spot at the focal point and was focused around the center of the channel. The beam was rotated by 4.46° about X-axis (see Figs. 1 and 2) in order to have Doppler frequency shift.

In order to detect Doppler frequency, the ODT system utilized the phase-resolved technique [9]. This technique took phase information derived from a Hilbert transformation to image flow. Since the technique utilized the phase change between sequential A-scans to construct velocity imaging, it decoupled spatial resolution and velocity sensitivity.

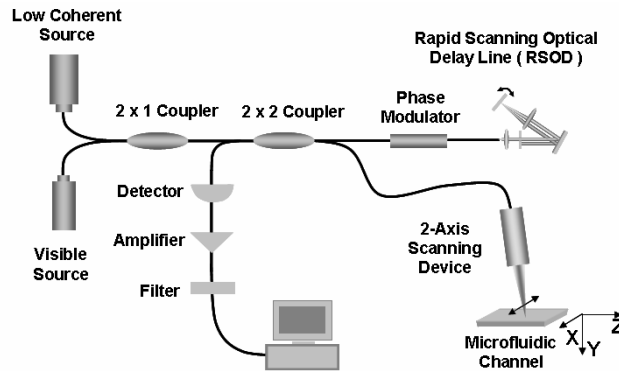


Fig. 2. Schematic diagram of the OCT/ODT system.

3. Experimental Results

Transient two-fluid mixing was observed at cross-section 1 as indicated in Fig. 1 (see movie files of Fig. 3). Five different Reynolds numbers were tested as shown in Table 1. An OCT/ODT probe scanned cross-section 1 along the upper blue line in Fig. 1. Initially, the entire channel was filled with particle/water mixture and the dual syringe pump was turned off. As soon as the pump was turned on with a programmed flow rate, OCT/ODT images were acquired at 1 frame per second. When the initial mixing was stabilized and reached a dynamic steady state, the pump was turned off again. Finally, the concentration reached a static steady state where scattering particles occupied the lower half cross-section which resulted from sedimentation.

As soon as the pump started to inject the water and particle/water mixture, the area filled with pure water (black area) increased with pressing the area with mixture (white area). The area occupied by the mixture rebounded and expanded to find a dynamic steady state. The rebounding center moved upward for a higher Reynolds number as shown in Fig. 3. In addition, because of the higher Reynolds number, dynamic steady state was reached faster.

At the dynamic steady state, sedimentation was observed macroscopically. Stratification between water and particle/water mixture was developed and a clear interface was observed in the transverse plane. OCT images shown in Fig. 4, which were taken from the movies of Fig. 3, represent the variation of interface orientation at dynamic steady states with respect to different sedimentation numbers. Interface orientation was defined by the angle between interface and horizontal (x) axis. As the sedimentation number decreased, the orientation increased to be saturated if the number was smaller than 1.08×10^{-5} . On the other hand, the orientation decreased along the streamwise (z) direction. The OCT/ODT probe was scanned along the blue lines in Fig. 1. Figure 5 shows the acquired OCT and ODT images at 15 cross-sections for $N_G = 1.08 \times 10^{-5}$. Interface orientation became 0° at cross-section 12 ($z \approx 200$). The

smaller the sedimentation number, the longer the streamwise distance was required for complete sedimentation. The Z-directional velocity component for $Re = 0.39$ (or $U = 648 \mu\text{m}/\text{sec}$) is clearly shown in ODT images. The distribution of its magnitude had a good agreement with the given average streamwise velocity. The changes of velocity direction in every other channel are represented by red (positive Z-direction, see Fig. 1) and blue (negative Z-direction). Vertical lines in ODT images were caused by the pulsating nature of the stepped motor in the syringe pump.

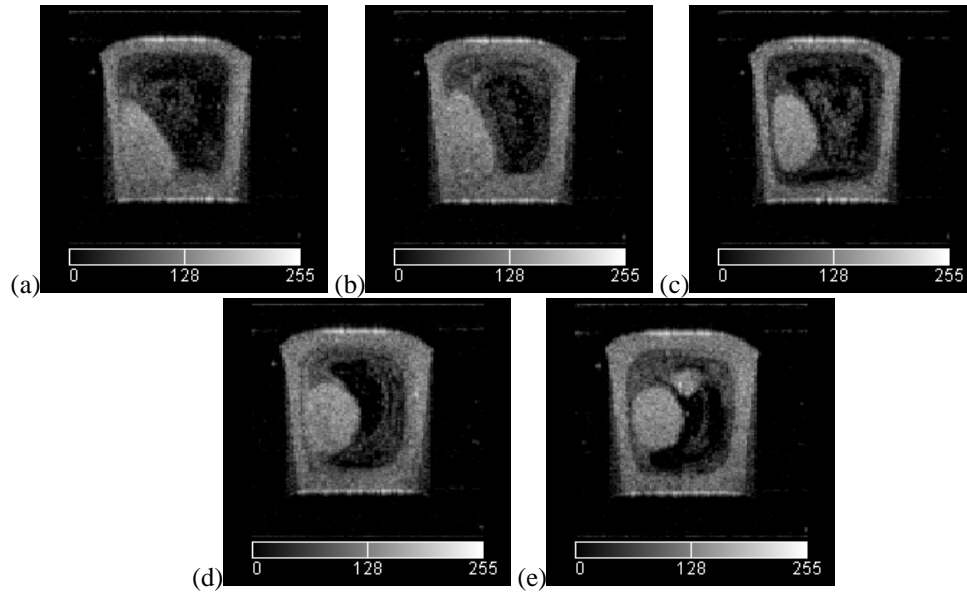


Fig. 3. Movies of transient two-fluid mixing with different Reynolds numbers. (a) $Re = 0.17$ (2.22MB or [6.97MB](#)), (b) $Re = 0.28$ (2.27MB or [7.02MB](#)), (c) $Re = 0.39$ (2.22MB or [6.88MB](#)), (d) $Re = 0.61$ (2.03MB or [6.61MB](#)), (e) $Re = 0.83$ (1.99MB or [6.47MB](#)).

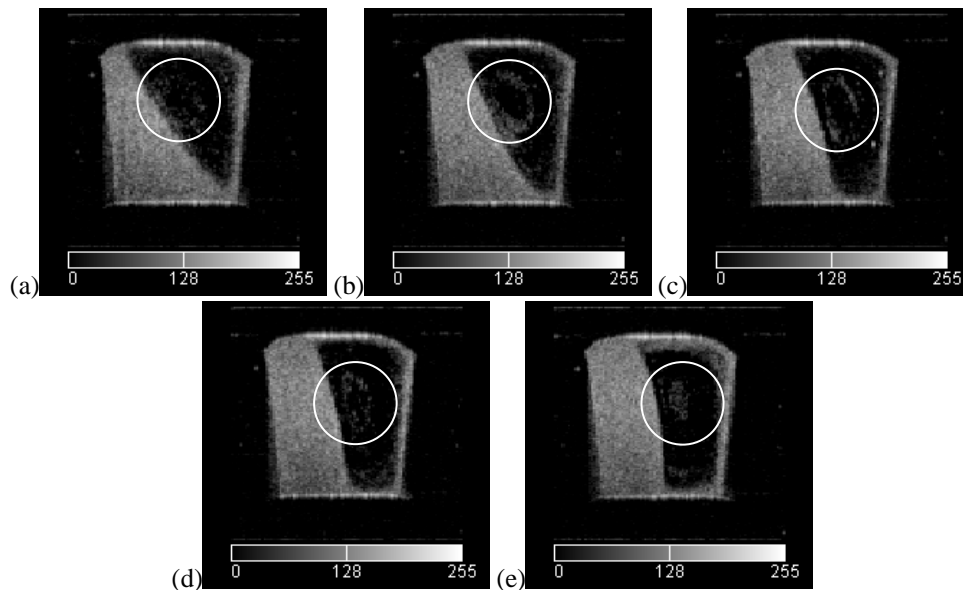


Fig. 4. Variation of interface orientation with respect to sedimentation numbers. (a) $N_G = 2.52 \times 10^{-5}$, (b) $N_G = 1.51 \times 10^{-5}$, (c) $N_G = 1.08 \times 10^{-5}$, (d) $N_G = 0.69 \times 10^{-5}$, (e) $N_G = 0.51 \times 10^{-5}$. Each circle indicates where secondary flow streamline is visualized.

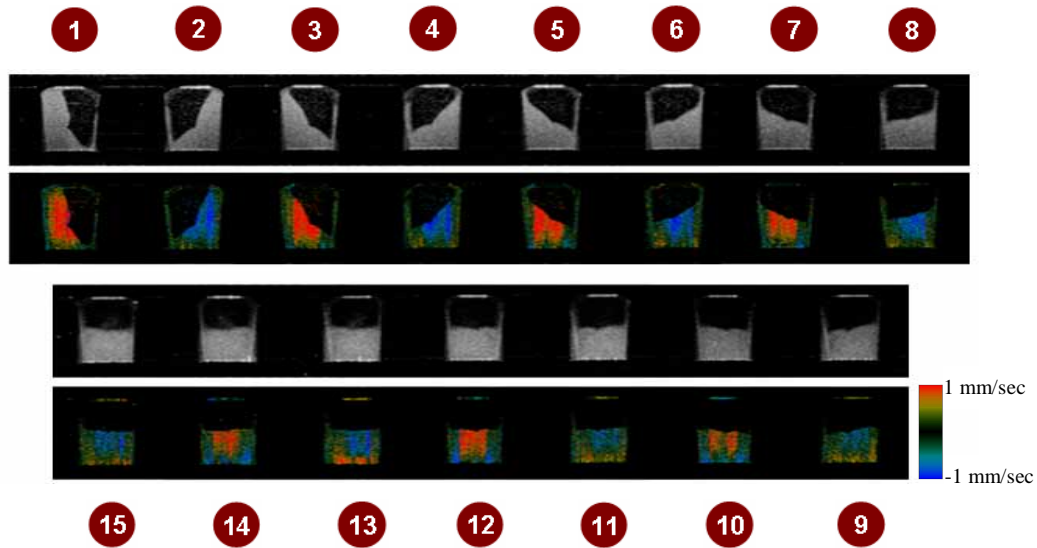


Fig. 5. OCT images for interface orientation (first and third rows) and ODT images for velocity component along Z-direction (second and fourth rows). The sedimentation number is 1.08×10^{-5} and the Reynolds number 0.39. The OCT/ODT probe is scanned along blue lines and the cross-section numbers are provided as shown in Fig. 1.

Finally, a three-dimensional volume image for OCT/ODT was taken along one loop of the serpentine channel, which was indicated with the red box in Fig. 1. The two-dimensional images were taken at every $10 \mu\text{m}$ slices, and total 350 slices was synthesized to construct the volume image of Fig. 6. The blue and red colors in the ODT image indicate the opposite direction of the fluid flow with respect to the probing beam direction.

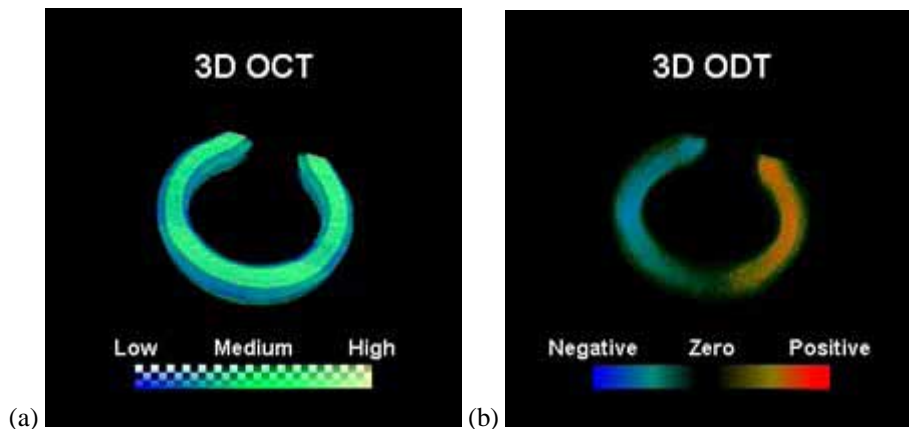


Fig. 6. Three-dimensional volume images for (a) OCT (859KB) and (b) ODT (587KB).

4. Discussions

Secondary flow, at the dynamic steady state, was observed as in the movie files of Fig. 3. Since secondary flow velocity had a three or four order smaller magnitude compared to streamwise velocity as shown in the previous section, it was difficult to observe using ODT.

Instead, OCT was used for the secondary flow visualization by imaging the movement of particles as a tracer.

Secondary flow caused by curving a channel has two identical vortices with opposite rotation in a transverse plane. The interface between two vortices is horizontal without sedimentation. However, upon introducing density difference, the secondary flow field was superposed by sedimentation-induced field. Since isoconcentration lines approached the superposed streamlines at high Dn^2Sc , the interface shown in Fig. 4 was expected to be identical to the interface between vortices. Because of low N_G , the effect of a sedimentation-induced velocity field on mixing was negligible.

The resultant secondary flow streamline was clearly observed in the area occupied by pure water (see the movie files in Fig. 3 and the indicating circles on Fig. 4). A small amount of particles was in a shape of elongated ring at the pure water side and the elongated ring was enlarged with time. The generation, enlargement, and disappearance of the ring were repeatedly observed and the life time was about 150 sec for Run 3.

The enlargement mechanism can be explained with a simple example. Suppose a particle packet is located at the center of the channel, the packet will be continuously dispersed by shear stress associated with the gradients of secondary and streamwise velocities. After a while, the shear dispersion will transform the packet to be two counter-rotating spiral curves on three-dimensional surface of 'camel humps' whose apexes are headed toward downstream. Each hump will be located at the pure water and the particle/water mixture sides respectively. An envelope containing two humps will approximately have a shape of Poiseuille velocity profile. Since the humps will be stretched along the streamwise direction with time by the gradient of streamwise velocity, an expanding ring can be observed at a transverse plane which is located at a downstream from the position the packet was released.

Even though OCT image could not show the expanding ring at the particle/water mixture side, there is the same mixing mechanism. The expanding mechanism can be described by neither a centrifugal force applied to particles nor a molecular diffusion because their time scales are much longer than the ring life time.

Since the secondary flow was negligible in steady-state, compared with the streamwise flow, ODT images in Figs. 5 and 6(b) represent the streamwise flow without a large error. Although the current ODT setup is only sensitive to the velocity component parallel to the line-of-sight, a multi-beam ODT with multiple Doppler angles can measure three-dimensional velocity field.

5. Conclusion

We assessed laminar dispersion in a serpentine microchannel. Since laminar dispersion was involved with complex 'convective diffusion' phenomena, it was essential that OCT/ODT had the unique feature to image structure and velocity at the same time. OCT, which has speckle contrast inherently, provided an excellent methodology to characterize a complex mixing structure and its time evolution. Since isoconcentration lines approach the secondary flow streamline in a transverse plane at high Dn^2Sc (this number is usually very high in common microfluidic experiments), OCT could visualize streamlines. We have analyzed OCT/ODT images in terms of streamwise velocity, secondary streamline, sedimentation time scale, and shear dispersion.

Acknowledgments

The authors would like to thank Dr. H. Takei for providing the testing sample and for helpful discussion. This work was supported by the Post-doctoral Fellowship Program of Korea Research Foundation (KRF-2004-214-D00202), the National Science Foundation (BES-86924), National Institutes of Health (EB-00255, NCI-91717, RR-01192), and the Air Force Office of Science Research (FA9550-04-1-0101). Institutional support from the Beckman Laser Institute Endowment is also gratefully acknowledged.